Multi-axial damage and failure of medical grade carbon fibre reinforced PEEK laminates: Experimental testing and computational modelling

Elizabeth Anne Gallagher[a], Steven Lamorinière[b], Patrick McGarry[a,*]

[a] Discipline of Biomedical Engineering, National University of Ireland Galway, University Road, Galway, Ireland
[b] Invibio Ltd., Hillhouse International, Thornton Cleveleys, Lancashire FY5 4QD, United Kingdom

ARTICLE INFO

ABSTRACT

Orthopaedic devices using unidirectional carbon fibre reinforced poly-ether-ether-ketone (PEEK) laminates potentially offer several benefits over metallic implants including: anisotropic material properties; radiolucency and strength to weight ratio. However, despite FDA clearance of PEEK-OPTIMA™ Ultra-Reinforced, no investigation of the mechanical properties or failure mechanisms of a medical grade unidirectional laminate material has been published to date, thus hindering the development of first-generation laminated orthopaedic devices. This study presents the first investigation of the mechanical behaviour and failure mechanisms of PEEK-OPTIMA™ Ultra-Reinforced. The following multi-axial suite of experimental tests are presented: 0° and 90° tension and compression, in-plane shear, mode I and mode II fracture toughness, compression of $\pm$ 45° laminates and flexure of 0°, 90° and $\pm$ 45° laminates. Three damage mechanisms are uncovered: (1) inter-laminar delamination, (2) intra-laminar cracking and (3) anisotropic plasticity. A computational damage and failure model that incorporates all three damage mechanisms is developed. The model accurately predicts the complex multi-mode failure mechanisms observed experimentally. The ability of a model to predict diverse damage mechanisms under multiple loading directions conditions is critical for the safe design of fibre reinforced laminated orthopaedic devices subjected to complex physiological loading conditions.

1. Introduction

To date PEEK-OPTIMA™ Ultra-Reinforced (Invibio Ltd., Thornton Cleveleys, UK) is the only unidirectional fibre reinforced thermoplastic material that has been cleared by the FDA for implantation in humans. However, no experimental characterisation of the material has been published and the failure mechanisms have not been uncovered. This presents a significant obstacle to the development of first-generation long unidirectional carbon fibre PEEK medical implants. This paper aims to address this key deficiency by presenting the first extensive experimental and computational investigation of the material behaviour and failure mechanisms of PEEK-OPTIMA™ Ultra-Reinforced.

Only a limited number of fibre reinforced composite medical implants are currently available. Short fibre and weaved glass fibre reinforced composites are being used in dental implants and craniofacial implants (Aitasalo et al., 2014; Ballo et al., 2007; Piitulainen et al., 2015), and neat PEEK and unaligned short fibre reinforced PEEK materials are currently used for a limited number of spinal and trauma

implants, such as vertebral cages and suture anchors (Brantigan and Steffee, 1993; Feerick et al., 2014, 2013a; Kurtz and Devine, 2007). However such neat PEEK and short carbon fibre reinforced PEEK composites are not suitable for fracture fixation devices due to low strength and stiffness (Gallagher et al., 2015). In contrast, laminated fracture fixation devices constructed from unidirectional long carbon fibre reinforced PEEK plies provide increased stiffness and strength along with tailorable anisotropic material properties. Development of first-generation orthopaedic fracture fixation devices using carbon fibre reinforced laminates potentially offer several benefits: (1) The effective anisotropic stiffness of a device can be designed to match that of the peri-prosthetic bone, reducing instances of bone resorption, which is a leading cause of metallic implant failure (Huiskes et al., 1992); (2) Unlike traditional materials, carbon fibre reinforced PEEK is radiolucent, thus avoiding the artefact caused by metal implants during CT imaging and X-rays and improving post-operative medical imaging (Kurtz and Devine, 2007); (3) The high strength to weight ratio of laminated devices will result in lighter and thinner implants compared to metallic equivalents, resulting in considerable improvement of patient

functionality and comfort; (4) Fibre reinforced composite implants will not induce patient pain and discomfort in cold weather, in contrast to metallic implants (Der Tavitian et al., 2002; Lanzetta and Foucher, 1995).

Identification of the complex failure mechanisms of laminated composites presents a significant challenge to the design and development of first-generation fibre reinforced laminated medical implants. A comprehensive characterisation of such failure mechanisms is particularly important for orthopaedic fracture fixation devices, given the complex multi-axial physiological loading environment post-implantation. Depending on the mode of loading, a combination of fibre failure, matrix failure, ply debonding and/or plasticity may occur. A number of well-established damage models have been proposed for failure of fibre reinforced laminates that take into account fibre and matrix failure in compression and tension, including Hashin (Hashin, 1980), Tsai-Wu (Tsai and Wu, 1971) and Puck (Puck and Schürmann, 2002). Recent finite element (FE) implementations incorporate the extended finite element method (XFEM) to predict crack propagation in conjunction with Hashin-type damage initiation criteria (Ahmad et al., 2014; Duarte et al., 2017; Feerick et al., 2013b). These modelling approaches focus solely on intra-laminar failure and do not consider inter-laminar delamination. Several experimental studies have shown that certain loading modes result in failure due to delamination, most notably tensile and compressive testing of laminates containing holes or arbitrarily angled plies (Lessard and Chang, 1991; O'Brien, 1982; Wisnom and Hallett, 2009). Various computational methodologies that include cohesive zone models (CZM) at the interface between the plies have been presented to predict inter-laminar failure (Heidari-Rarani et al., 2013; Turon et al., 2010; Zhao et al., 2014). Most recently, models have been proposed that implement both inter- and intra- laminar failure in a combined XFEM/CZM modelling methodology (Bieniaś et al., 2012; Bouhala et al., 2015; Grogan et al., 2015a; Vigueras et al., 2015). Finally inelastic permanent plastic deformation has been observed in several experimental studies of fibre reinforced laminates (Soden et al., 2004; Van Paepegem et al., 2006). However the plastic deformation of fibre reinforced laminates has seldom been considered computationally. Vogler et al. (Vogler et al., 2013) identified the need for a constitutive model that is capable of predicting non-linearities under multi-axial and tri-axial stress states. van der Meer et al. (van der Meer et al., 2011) has presented an implicit XFEM/CZM methodology that includes plasticity but only considers the off-axis non-linear responses in one loading direction and does not make reference to the anisotropic nature of the plasticity response of fibre reinforced laminates. In the current study a combined extended finite element method and cohesive zone model (XFEM/CZM) is developed to simulate the formation of random 3D crack paths, the growth inter-ply delaminations and anisotropic plasticity of the fibre reinforced laminates.

The current paper presents the first comprehensive experimental characterisation of the mechanical behaviour and failure mechanisms of a medical grade unidirectional carbon fibre reinforced PEEK material, PEEK-OPTIMA™ Ultra-Reinforced, hereafter referred to as *CF/PEEK*. Based on experimental data, a computation framework is developed so that material failure due to intra-laminar cracking, inter-laminar delamination, and anisotropic plasticity is predicted. Finally, a preliminary device design study is carried out to demonstrate the potential of the developed computational framework as a design tool for future laminated implants. Such comprehensive experimental data and multi-mode damage modelling is essential for the development of first-generation laminated fracture fixation devices due to the complex multi-axial physiological loading environment encountered post-implantation. The paper is structured as follows: Section 2 - Experimental methods; Section 3 - Computational model development; Section 4 - Experimental results and model calibration; Section 5 - Analysis of failure modes and model validation; and Section 6 - Preliminary laminated device design.

2. Experimental methods

CF/PEEK is a medical grade poly-ether-ether-ketone (PEEK) polymer reinforced with continuous unidirectional carbon fibres, with a 62% fibre volume fraction. As mentioned in the introduction, to date no experimental data has been published for *CF/PEEK*. In order to determine the transversely isotropic moduli and failure strengths of the *CF/PEEK* material, uniaxial tension and compression tests were performed on 0°, 90° and ± 45° specimens. All the experiments performed in this study comply with the ASTM or ISO standards. The authors are not aware of other works that provide such extensive experimental testings.

2.1. Specimen preparation

CF/PEEK prepreg, which has a thickness of 0.2 mm, was consolidated into a number of laminated panels with angled plies according to ASTM D5687. Compression moulding was used to consolidate the ± 45° laminates, while the 0° and 90° laminated panels were consolidated in an autoclave. The resulting thickness of the laminated plates was dependent on the number of plies in the layup.

Test specimens were cut from the laminated panels using a composite cutting machine with a diamond-coated cutting blade. The specimen geometries were in accordance with their respective test standards (Tensile: ASTM D3039-07 (ASTM International, 2014), Compression: ASTM D6641-14 (ASTM International, 2012), Flexure: ISO 14125–98 (ISO, 1998), In-Plane Shear: ASTM D3518-13 (ASTM International, 2013), Mode I and II fracture toughness tests: EN6033-95 and EN6034-95 (AECMA Standard, 1995a, 1995b). The exact specimen dimensions for each experiment are listed in Table A1 in the appendix of this study. For each mode of loading 5 test specimens were tested in accordance with the standards, in total 75 test specimens were prepared.

For the tension, compression and in-plane-strain experiments, cross gauges were attached to the specimens to measure strains in the longitudinal and transverse directions. In accordance with the standards a linear gauge was also attached to the opposite face of the specimen to simultaneously measure the longitudinal strain on both faces and allow for detection of any bending that may occur during testing. A camera system was used to measure deformation in the flexure tests (1.31 MPa, 25 fps; uEye, IDS, Obersulm, Germany; videoXtens software, Zwick, Ulm, Germany).

2.2. Testing

The loading rates and machines used for each experiment are next presented. The 0° tensile specimens and the in-plane-shear ± 45° specimens were monotonically loaded in a Denison Meyer T.24.B.4 machine (with a 500 kN load cell). The 90° tensile tests were performed on a 4467 Screw Driven Instron (30 kN load cell). A displacement rate of 2 mm/min was implemented for all tests. The four-point-bend flexure tests were also carried out on a 4467 Screw Driven Instron at a rate of 2 mm/min. All the compression specimens were mounted in a combined loading compression test fixture and loaded to failure on a Zwick Z250 testing machine (with a 250 kN load cell) at a nominal rate of 1.3 mm/min. The fracture toughness tests were performed on a Zwick Z010 testing machine (10 kN load cell) with crosshead displacement rates of 10 mm/min and 1 mm/min for the G_{ic} and G_{iic} tests, respectively.

3. Computational model development

Due to the complex multi-axial loading environment encountered by fracture fixation devices a predictive modelling framework must be developed that incorporates inter-laminar failure, intra-laminar failure and laminate plasticity. As will be shown in the experimental results in

Sections 4 and 5 of this paper, a combination of all three failure mechanisms may occur in *CF/PEEK*. Furthermore, a study of neat PEEK (Rae et al., 2007) shows that the matrix material exhibits inelastic plastic material behaviour under compressive and tensile loading. In Section 3.1 we outline a plasticity formulation to simulate permanent anisotropic deformation of the unidirectional fibre reinforced material. In Section 3.2 we outline the mixed mode traction separation relations governing delamination in the laminates. Finally, in Section 3.1 the Hashin-type intra-laminar damage initiation criteria are outlined. To the best of the author's knowledge the modelling framework presents the first combination of anisotropic plastic laminar deformation, mode dependent inter-laminar failure and intra-laminar failure.

3.1. Simulating anisotropic plasticity of composite structures

Previous models have implemented isotropic plasticity in their computational damage model but the experimental results in this study clearly point to an anisotropic inelastic plastic response of the laminates. The yield behaviour of the laminate is simulated using Hill's potential function. The yield criterion is expressed below in terms of Cauchy stress components.

$$f(\sigma) = \left(\sqrt{F(\sigma_{22} - \sigma_{33})^2 + G(\sigma_{33} - \sigma_{11})^2 + H(\sigma_{11} - \sigma_{22})^2 + 2L\sigma_{23}^2 + 2M\sigma_{31}^2 + 2N\sigma_{12}^2} \right)$$
$$- \sigma_{yield} = 0 \tag{1}$$

where, F, G, H, L, M, and N are constants obtained from experimental testing of the material. They are defined as follows:

$$F = \frac{(\sigma_{yield})^2}{2} \left(\frac{1}{\sigma_{22}^2} + \frac{1}{\sigma_{33}^2} - \frac{1}{\sigma_{11}^2} \right) = \frac{1}{2} \left(\frac{1}{R_{22}^2} + \frac{1}{R_{33}^2} - \frac{1}{R_{11}^2} \right) \tag{2}$$

$$G = \frac{(\sigma_{yield})^2}{2} \left(\frac{1}{\sigma_{33}^2} + \frac{1}{\sigma_{11}^2} - \frac{1}{\sigma_{22}^2} \right) = \frac{1}{2} \left(\frac{1}{R_{33}^2} + \frac{1}{R_{11}^2} - \frac{1}{R_{22}^2} \right) \tag{3}$$

$$H = \frac{(\sigma_{yield})^2}{2} \left(\frac{1}{\sigma_{11}^2} + \frac{1}{\sigma_{22}^2} - \frac{1}{\sigma_{33}^2} \right) = \frac{1}{2} \left(\frac{1}{R_{11}^2} + \frac{1}{R_{22}^2} - \frac{1}{R_{33}^2} \right) \tag{4}$$

$$L = \frac{3}{2} \left(\frac{\tau_{yield}}{\sigma_{23}} \right)^2 = \frac{3}{2R_{23}^2} \tag{5}$$

$$M = \frac{3}{2} \left(\frac{\tau_{yield}}{\sigma_{13}} \right)^2 = \frac{3}{2R_{13}^2} \tag{6}$$

$$N = \frac{3}{2} \left(\frac{\tau_{yield}}{\sigma_{12}} \right)^2 = \frac{3}{2R_{12}^2} \tag{7}$$

where each σ_{ij} is the measured yield stress value under a uniaxial load in the *ij* direction; σ_{yield} is the reference yield stress; R_{ij} are the anisotropic yield stress ratios and $\tau_{yield} = \frac{\sigma_{yield}}{\sqrt{3}}$. The anisotropic yield ratios are determined from the results of the uniaxial experimental tests performed on the 0°, 90° and ± 45° laminates.

3.2. Simulating inter-laminar delamination

The results of the G_{ic} and G_{iic} fracture toughness tests presented in Section 4 provide motivation for a mode dependent CZM formulation. Inter-laminar failure is governed by the traction separation relations defined in Eqs. 8–11 below. Delaminations can occur in the laminate if the interface traction exceeds a critical value of σ_{max} in mode I and τ_{max} in mode II.

when $\Delta_n > 0$,

$$T_n(\Delta_n, \Delta_t) = \sigma_{max} exp(1) \left(\frac{\Delta_n}{\delta_n} \right) exp \left(-\sqrt{\frac{\Delta_n^2}{\delta_n^2} + \frac{\Delta_t^2}{\delta_t^2}} \right) \tag{8}$$

$$T_t(\Delta_n, \Delta_t) = \tau_{max} exp(1) \left(\frac{\Delta_t}{\delta_t} \right) exp \left(-\sqrt{\frac{\Delta_n^2}{\delta_n^2} + \frac{\Delta_t^2}{\delta_t^2}} \right) \tag{9}$$

when $\Delta_n < 0$,

$$T_n(\Delta_n, \Delta_t) = \sigma_{max} exp(1) \left(\frac{\Delta_n}{\delta_n} \right) exp \left(-\sqrt{\frac{\Delta_n^2}{\delta_n^2}} \right) \tag{10}$$

$$T_t(\Delta_n, \Delta_t) = \tau_{max} exp(1) \left(\frac{\Delta_t}{\delta_t} \right) exp \left(-\sqrt{\frac{\Delta_t^2}{\delta_t^2}} \right) \quad exp \left(-\beta \frac{\Delta_n}{\delta_n} \right) \tag{11}$$

where, σ_{max} is the maximum normal traction (referred to hereafter as the "mode I interface strength"), τ_{max} is the maximum tangential traction (referred to hereafter as the "mode II interface strength"), Δ_n and Δ_t are the normal and tangential components of the interface separation vector Δ, respectively and δ_n and δ_t are the normal and tangential interface characteristic lengths, respectively, and the coupling parameter β is set to 0.4 (McGarry et al., 2014). The normal (mode I) work of separation is given as $\phi_n = \sigma_{max}\Delta_n exp(1)$ and the tangential (mode II) work of separation is given as $\phi_t = \tau_{max}\Delta_t exp(1)$.

Two sets of normal and tangential traction equations are presented. When the model undergoes normal tensile separation Eqs. (8) and (9) are implemented, where both the normal and the tangential interface tractions, T_n and T_t, are coupled by the effective separation parameter $(\Delta_n^2/\delta_n^2 + \Delta_t^2/\delta_t^2)$. Eqs. (10) and (11) prevent overclosure during normal compression of the interface, while allowing shear delamination. This CZM was developed by McGarry et al. (2014) and is implemented through a user defined interface subroutine (UINTER). A parametric study was performed to determine the required element length to provide a converged solution of crack propagation rate and fracture toughness. Convergence is achieved using an element length of 33 μm.

3.3. Simulating intra-laminar failure

A multi-axial failure criterion with a continuum representation of intra-laminar failure that may result from fibre rupture and/or matrix cracking is presented. Here two failure mechanisms are considered when modelling the inter-laminar failure of fibre reinforced laminates, failure of the fibres and failure of the matrix material. The Hashin-type damage initiation criteria (Hashin, 1980) are outlined in Eqs. (12)–(15) below. The equations describe both fibre (f^f) and matrix (f^m) failure of the laminate in tension (f_T) and compression (f_C). Once any of the failure criteria reaches a value of 1, damage is initiated for that criterion and a crack will occur. The four anisotropic damage initiation criteria used in this model are described as follows:

$$f_T^m = \left(\frac{\sigma_{11}}{Y_T} \right)^2 + \left(\frac{\sigma_{12}}{S} \right)^2 + \left(\frac{\sigma_{13}}{S} \right)^2 \tag{12}$$

$$f_C^m = \left[\left(\frac{Y_C}{2S_{23}} \right)^2 - 1 \right] \left(\frac{\sigma_{22} + \sigma_{33}}{Y_C} \right) + \frac{(\sigma_{22} + \sigma_{33})^2}{4S^2} + \frac{\sigma_{23}^2 - \sigma_{22}\sigma_{33}}{S^2}$$
$$+ \frac{\sigma_{12}^2 + \sigma_{13}^2}{S^2} \tag{13}$$

$$f_T^f = \left(\frac{\sigma_{11}}{X_T} \right)^2 + \left(\frac{\sigma_{12}}{S} \right)^2 + \left(\frac{\sigma_{13}}{S} \right)^2 \tag{14}$$

$$f_C^f = \left(\frac{\sigma_{11}}{X_C} \right)^2 + \left(\frac{\sigma_{12}}{S} \right)^2 + \left(\frac{\sigma_{13}}{S} \right)^2 \tag{15}$$

where, X_T and X_C are the longitudinal tensile and compressive strengths, respectively, and Y_T and Y_C are the transverse tensile and compressive strengths, respectively and S is the shear strength of the laminate. The fibre and matrix failure criteria are implemented through a user defined damage initiation subroutine (UDMGINI). Following initiation, XFEM (Feerick et al., 2013b) is used to simulate the

propagation of the crack through the laminate. Once the prescribed fracture criterion has been reached the real nodes and corresponding phantom nodes will separate and allow the crack to propagate.

4. Experimental results and computational model calibration

The following section presents the results for the experimental tests that are performed on the *CF/PEEK* laminates. Importantly experimental observations are used to develop and calibrate our computational model. Compression tests are performed on 90° laminates to measure the transverse ultimate compressive strength. Tensile tests are performed on 0° and 90° laminates in order to determine the longitudinal modulus and ultimate tensile strength and the transverse modulus and ultimate tensile strength, respectively. The mode I and mode II inter-laminar strengths are determined through fracture toughness test carried out on a 0° laminate manufactured with a pre-crack. Compression tests are also carried out on 0° laminates to measure the longitudinal ultimate compressive strengths. Flexure tests are performed on 0°, 90° and ± 45° laminates and compression tests are performed on ± 45° laminates. In-plane shear tests performed on ± 45° are used to measure the shear modulus and shear strength of the *CF/PEEK* composite material. All of the tests are modelled in the commercial finite element software Abaqus 6.13 (SIMULIA, Providence, RI, USA) and calibrated using the results of the experiments. The experimental stress-strain diagrams and experimental images of failure surfaces are presented as a critical input and motivation for the computational model development and calibration.

4.1. Experimental measurement of elastic constants and failure strengths and fracture toughness

The transversely isotropic properties of unidirectional *CF/PEEK* that are determined experimentally through tensile tests performed on 0°, 90° and ± 45° specimens are presented in Table 1 below.

The measured longitudinal modulus E_{11}, i.e. the modulus in fibre direction, is an order of magnitude greater than the transverse modulus E_{22}, i.e the modulus in the matrix direction. The longitudinal modulus is slightly higher than typical values for non-medical grades of carbon fibre reinforced PEEK laminates, which are reported to be in the range of 135 – 155 GPa. Similarly, the measured Poisson's ratio value of 0.38 is higher than other reported values, 0.32–0.34. However, both the transverse modulus and the shear modulus for *CF/PEEK* are in good agreement with the values reported for other grades of CF/PEEK laminates (Grogan et al., 2015b; Li et al., 2002).

The failure strengths for *CF/PEEK* are given in Table 2, where X_T and X_C are the longitudinal tensile and compressive strengths, respectively, Y_T and Y_C are the transverse tensile and compressive strengths, respectively and S is the shear strength.

The measured longitudinal tensile strength, X_T, of 2882 MPa is greater than values for other grade of unidirectional CF/PEEK reported in the literature (2068 MPa (Li et al., 2002)). Both the transverse tensile strength, Y_T, and the transverse compressive strength, Y_C, 50 MPa and 213 MPa respectively, are similar to other grades of CF/PEEK materials (Grogan et al., 2015b) but at the lower end of the range of transverse strengths for other carbon fibre reinforced polymers (O'Higgins et al., 2008). It should be noted that there is no polymer sizing on the fibres in

Table 1
CF/PEEK tensile material properties (mean ± standard deviation).

$E_{11}(GPa)$	175.37 ± 5.61
$E_{22}(GPa)$	9.40 ± 0.16
$G_{12}(GPa)$	5.21 ± 0.19
v_{12}	0.38 ± 0.04

Table 2
CF/PEEK tensile, compressive and shear strengths and mode I and mode II fracture toughness (mean ± standard deviation).

$X_T(MPa)$	2882.09 ± 98.25
$Y_T(MPa)$	49.60 ± 3.92
$X_C(MPa)$	1182.26 ± 67.99
$Y_C(MPa)$	185.69 ± 8.92
$S(MPa)$	95.83 ± 7.44
$G_{ic}(kJ/m^2)$	1.44 ± 0.10
$G_{iic}(kJ/m^2)$	1.01 ± 0.03

the *CF/PEEK* material tested, as there is no known sizing that is fully compatible with PEEK. Sizing is a coating added to the carbon fibres to improve fibre-matrix interface strength (Pozegic et al., 2016), which would significantly increase the laminates transverse strengths. The shear strength, *S*, of *CF/PEEK*, measured as 96 MPa falls within the range of values reported for other grades of CF/PEEK unidirectional laminates (Grogan et al., 2015b; Li et al., 2002).

4.2. Analysis of compressive failure of 90° laminates

Experimental results and computational analysis for compression tests performed on 90° laminates are presented in Fig. 1. The experimental and computational stress-strain diagrams are shown in Fig. 1 (A).

The experimental stress-strain curves exhibit an initial linear-elastic region up to a yield stress of 110 MPa. Following the initial yield point the specimens undergo strain hardening up to the ultimate compressive failure stress. Our computational model provides an accurate prediction of the initial elastic behaviour, post yield hardening and ultimate failure. The computed stress (176.6 MPa) and strain (0.028) at failure are similar to the experimentally observed values of 185.69 ± 8.92 MPa and 0.0266 ± 0.0044, respectively. This suggests that the transverse compressive strength, Y_C, represents a ductile failure of the matrix.

The computed compressive failure mode of the 90° laminate is shown in Fig. 1 (B). The crack initiates on the x-z face of the specimen. As shown in the inset of Fig. 1 (Bii) 'V-shaped' shear cracks are computed. The cracks propagate through the laminate in the y-direction until ultimate failure, as shown in Fig. 1 (Biii). The ± 45° shear cracks on the xz-plane are observed experimentally, as shown in Fig. 1 (C). The crack propagation through the specimen in the y-direction is also evident.

4.3. Analysis of tensile failure of 0 and 90 laminates

The experimental results and computational predictions for tensile tests performed on 0° and 90° laminates are presented in Figs. 2 and 3 below, respectively.

Fig. 2 (A) shows the stress-strain diagram for the 0° tensile test. A linear elastic regime is observed up to the point of longitudinal tensile strength, X_T, of 2765.14 ± 274.98 MPa at a strain of 0.012 ± 0.001. The computational model provides a good prediction of the experimental stress-strain behaviour. The absence of plastic deformation is correctly predicted by the computational model due to the high value of R_{11} in the Hill model, resulting in ultimate longitudinal tensile failure before yielding is predicted. This demonstrates the importance of anisotropic plasticity when modelling fibre reinforced laminates because, if for example the 90° Hill ratio, $R_{22} = 1$, was applied to the 0°laminate the model would predict nonlinear behaviour in the 0° tension prior to ultimate failure, which is not observed experimentally. The crack predicted by the computational model initiates at 45° due to stress concentrations caused by the constraint of the tabs, shown in Fig. 2 (Cii).
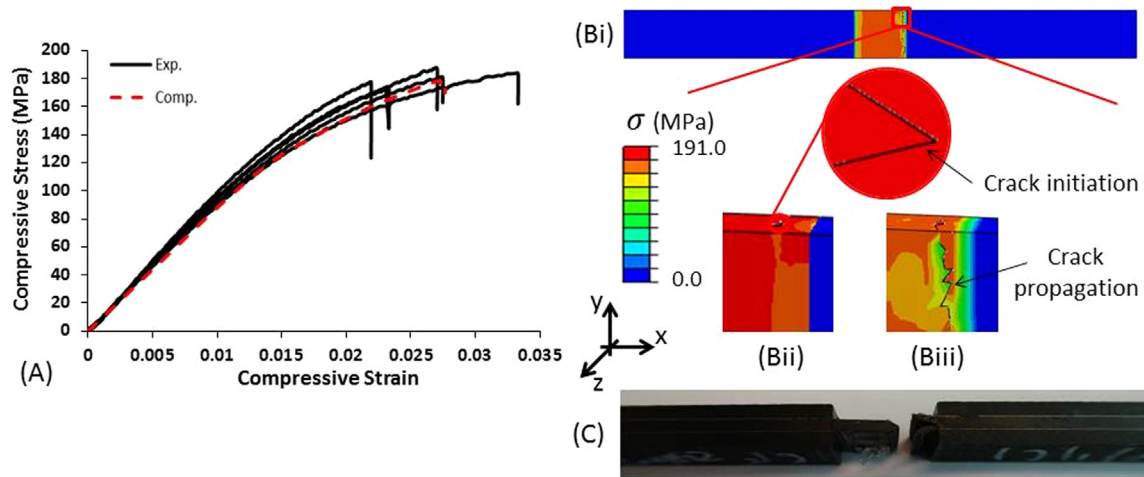
Fig. 1. (A) Experimental and computational nominal stress - nominal strain curves for compression of 90° laminates. (Bi) Von Mises stress (σ) distribution in the 90° laminate at failure. (Bii) Predicted crack at the point of initiation. (Biii) Propagated crack at the point of failure. (C) Experimental image of a failed specimen highlighting shear crack failure surfaces.

Following initiation, the crack is computed to 'kink' and propagate through the laminate in the y-direction (Fig. 2 (Ciii)). Comparing with the experimental image (Fig. 2 (B)) it is clear that the computational model predicts the propagated crack very accurately.

Fig. 3 (C) shows the stress-strain diagram for tensile testing of 90° laminates. The experimental results exhibit linear elastic behaviour up to the transverse tensile strength, Y_T, of 49.60 $\pm$ 3.95 MPa at a strain of 0.0054 $\pm$ 0.0005. Unlike the compressive testing of 90° laminates, shown in Fig. 1 (A) above, plasticity is not observed in the tensile test. This is correctly predicted by the computational model, in which the transverse failure strength, Y_T, is reached before plastic yielding can occur. This result suggests that failure during transverse tensile tests, characterised by Y_T, is due to debonding of the fibre-matrix interface rather than plastic yielding and ductile failure of the matrix. In the experimental image (Fig. 3 (B)) there is no evidence of fibrillation on the crack surface further supporting the proposed failure mechanism of fibre-matrix debonding. Fig. 3 (Ci) shows the predicted stress distribution at failure in the computational simulation. The model accurately predicts the crack location and the propagation through the laminate in the y-direction.

4.4. Analysis of the G_{ic} and G_{iic} fracture toughness tests

Results for the mode I (Fig. 4) and the mode II (Fig. 5) fracture toughness tests are presented.

Fig. 4 (A) shows the measured force-displacement curves for the mode I fracture toughness tests, from which a G_{ic} value of 1299.13 $\pm$ 92.77 J/m^2 is determined. Computational simulation of this mode I fracture tests accurately predicts the force-displacement behaviour and G_{ic} value when a cohesive zone mode I strength of $\sigma_{max} = 49.5$MPa is used with a characteristic interface length of $\Delta_n = 0.01\mu m$, so that $\phi_n = 1341 J/m^2$. A parametric investigation of the influence of cohesive zone model parameters and inter-laminar delamination is presented in Appendix B. The CZM simulation of delamination propagation provides an accurate prediction of the measured force-displacement relationship with an initial drop in force followed by a plateau during steady state crack propagation. The experimental results reveal that a propagated crack of 100 mm is achieved for an applied crosshead displacement of 38.77 $\pm$ 1.34 mm. Such crack propagation is accurately predicted by the computational model with a crack of 100 mm computed at an applied end displacement of 37.6 mm.
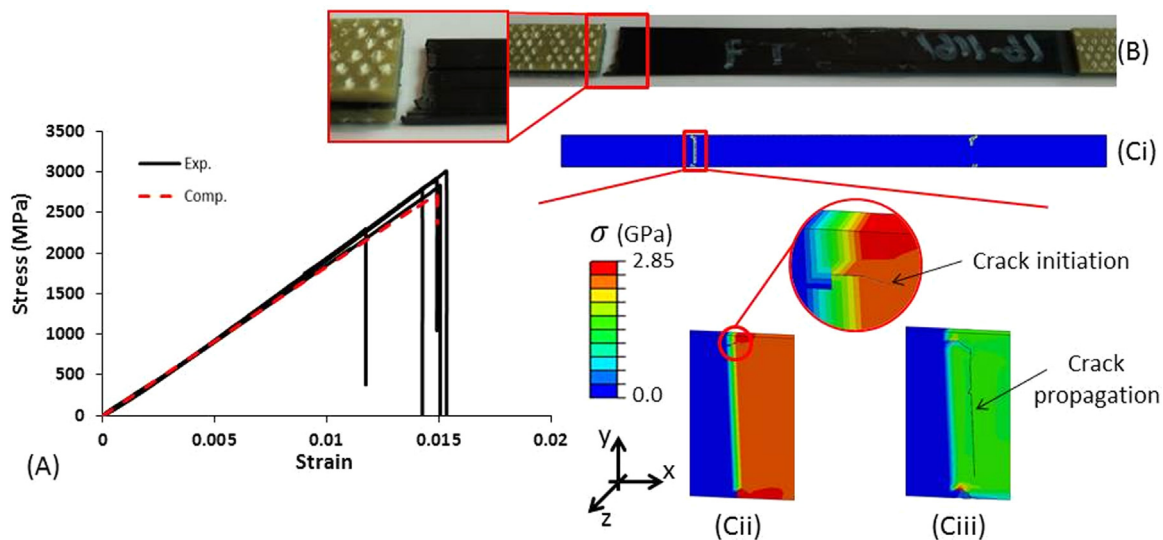

Fig. 2. (A) Experimental and computational nominal stress - nominal strain curves for the tensile tests of 0° laminates. (B) Experimental image of a 0° tensile specimen. (Ci) Predicted von Mises stress (σ) distribution in a 0° laminate. (Cii) Von Mises stress (σ) distribution in the 0° laminate at the point of crack initiation. (Ciii) Propagated crack in the 0° laminate at failure.
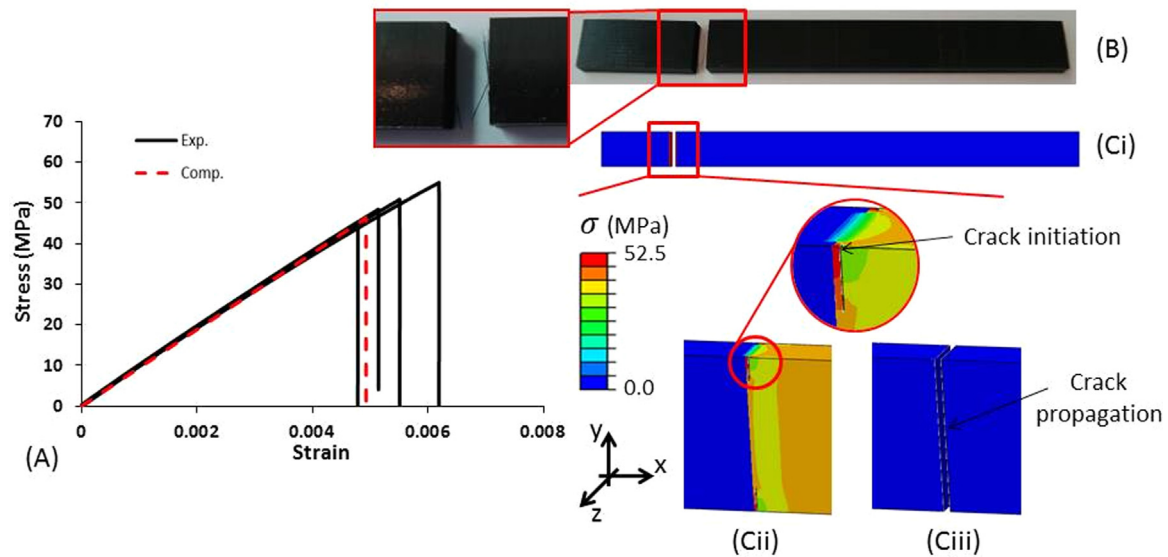
Fig. 3. (A) Experimental and computational nominal stress - nominal strain curves for the tensile tests of 90° laminates. (B) Experimental image of a 90° specimen following failure. (Ci) Predicted von Mises stress (σ) distribution in the 90° laminate at failure. (Cii) Predicted stress state following crack initiation. (Ciii) Predicted crack propagation at ultimate failure.
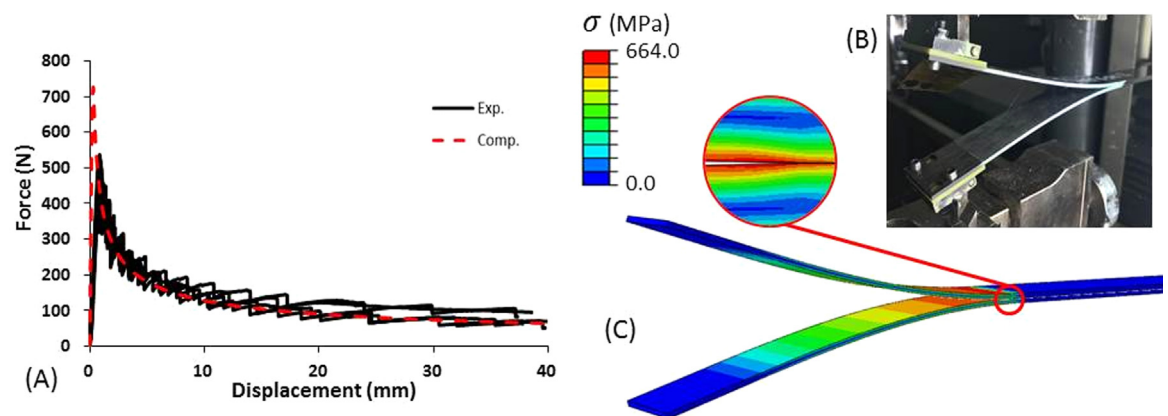

Fig. 4. (A) Experimental and predicted force-displacement curves for mode I fracture toughness tests. B) Experimental image of the mode I crack propagation. (C) Predicted crack propagation and von Mises stress (σ) distribution in the mode I fracture toughness tests.
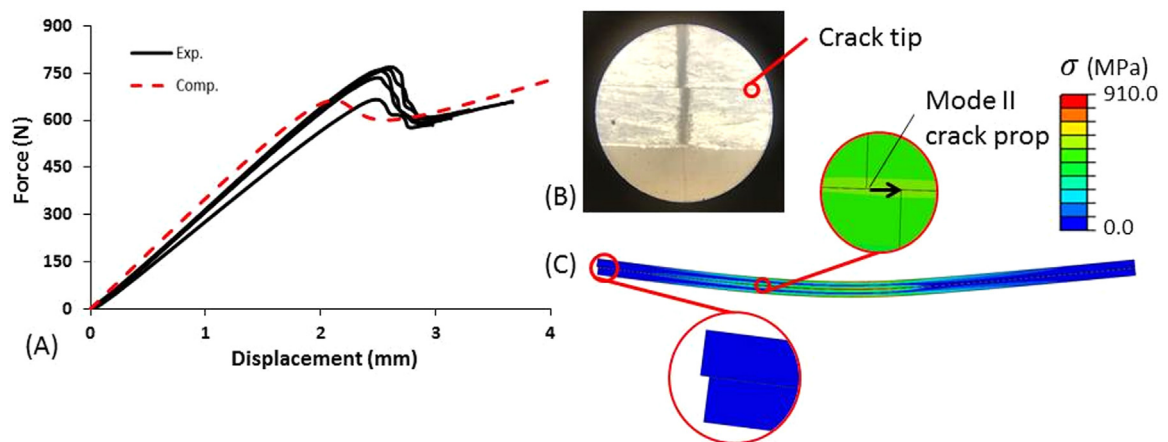

Fig. 5. (A) Experimental and predicted force-displacement curves for mode II fracture toughness tests. B) Experimental image of the mode II crack propagation. (C) Predicted crack propagation and von Mises stress (σ) distribution in the mode II fracture toughness tests.

Fig. 4 (B) shows a experimentally deformed specimen at a crack propagation of 100 mm. Fig. 4 (C) shows the stress distribution in the computed deformed specimen. Finally, it is interesting to note that the calibrated mode I inter-laminar strength, σ_{max}, is equal in value to the transverse tensile strength, Y_T, measure in tensile tests of 90° laminates. In both cases the failure stress is lower than the calibrated yield stress (110 MPa), see Fig. 1 (A), suggesting that fibre-matrix debonding is the underlying failure mechanism in both mode I inter-laminar delamination and intra-laminar transverse tensile failure.

Fig. 5 (A) shows the experimental force-displacement curves for the mode II fracture toughness tests. The experimental G_{iic} is determined as $1007.01 \pm 71.43 \, J/m^2$. Computational simulation of this mode II fracture tests accurately predicts the G_{iic} value when a cohesive zone mode II strength of $\tau_{max} = 37 \, MPa$ is used with a characteristic interface length of $\Delta_t = 0.01 \mu m$, so that $\phi_t = 1003 \, J/m^2$ (results of the parametric investigation are presented in Appendix B). These values give a reasonable replication of the experimentally observed force-displacement curve (Fig. 5 (A)) with an initial linear region followed by a drop in the force as the crack propagation begins. Fig. 5 (B) shows an experimental image of the mode II crack viewed through a microscope. The tip of the crack is highlighted. The vertical line (thick black line) used to mark the tip of the crack prior to testing is visible. Crack propagation is taken to initiate once a discontinuity appears in this marker. Fig. 5 (C) shows the predicted stress distribution in the G_{iic} fracture toughness test. The propagation of the mode II crack is highlighted.

4.5. Analysis of the compression failure of 0° laminates

The results for the compression tests performed on the 0° laminates are outlined in Fig. 6.

Fig. 6 (A) shows the stress-strain diagram for the 0° compression tests. Linear-elastic behaviour up to a nominal axial compressive strain of 0.0055 is observed. At strains in the region of 0.005–0.006, all experimental specimens experience a small drop in force before continuing to deform linearly up to a longitudinal compressive strength, X_Y, of $1182.26 \pm 67.99 \, MPa$. The slight drop in stress coincides with the point of tab detachment. The computational model predicts a linear stress-strain response up to the ultimate compressive strength of the 0° laminate at 1036.4 MPa at a strain of 0.0061. Tab detachment is not included in the model therefore the discontinuity in the stress response is not predicted prior to ultimate failure. Fig. 6 (Bii) shows the location for the predicted crack initiation on the edge of the laminate. The crack propagates through the laminate in the y-direction until ultimate failure, Fig. 6 (Biii).

Table 3
Calibrated material parameters for *CF/PEEK*.

Hill's potential function	R_{11}		250
	R_{22},	R_{33}	1.0
	R_{12},	R_{13}	0.64
	R_{23}		1.0
Cohesive zone model	σ_{max} (MPa)		49.5
	τ_{max} (MPa)		37
	δ_n (μm)		0.01
	δ_t (μm)		0.01

4.6. Summary of calibrated model parameters

Plasticity and damage model parameters for *CF/PEEK* are listed in Table 3 below. Additionally, intra-laminar failure model parameters are taken directly from experimental results in Table 2 and material and elastic properties are taken from experimental values listed in Table 1.

5. Model validation

Using the model parameters calibrated in the previous section we next assess the ability of the model to predict a variety of failure patterns. Specifically, we consider flexure tests of 0° and 90° laminates, compression and flexure tests of ± 45° laminates and in-plane shear tests of ± 45° laminates.

5.1. Predicting failure in 0° and 90° laminates under flexure loads

The flexural modulus and strength measured from four-point-bend tests performed on 0° and 90° laminates are presented in Table 4 below.

Fig. 7 (A) shows the force-displacement curves for 0° flexure tests. The force increases linearly to a failure load of $918.11 \pm 36.71 \, N$ at an applied displacement of $7.61 \pm 0.92 \, mm$. The computational model provides a good prediction of the force-displacement relationship with a computed failure load of 940.99 N at a displacement of 7.05 mm. An experimental image of the 0° flexure specimen in Fig. 7 (C), exhibits inter-laminar delamination in addition to crack propagation in the vicinity of the load points on both the compressive and tensile sides of the specimen. The computational model correctly predicts the simultaneous evolution of these two modes of damage as shown in Fig. 7 (B).

Fig. 7 (D) shows a linear force-displacement relationship for the 90° flexure tests up to an ultimate failure load of $145.37 \pm 11.79 \, N$ at an applied displacement of $1.93 \pm 0.17 \, mm$. The computational model accurately predicts this linear behaviour, with a computed failure load
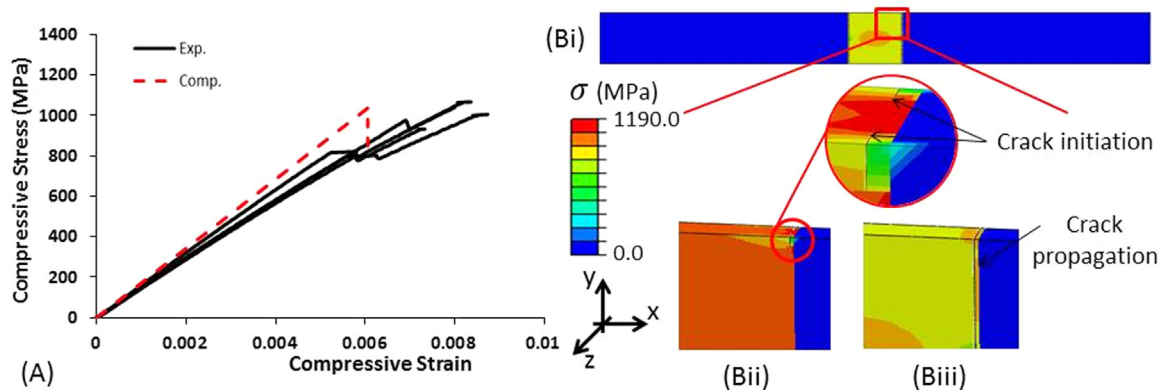

Fig. 6. (A) Experimental and computational nominal stress - nominal strain curves for the compression of 0° laminates. (Bi) Predicted von Mises (σ) stress distribution in failed 0° laminate. (Bii) Stress distribution at the point of crack initiation. (Biii) Von Mises stress (σ) distribution at the point of compressive failure following crack propagation.

Table 4
Flexural modulus and strength of the 0° and 90° laminates (mean ± standard deviation).

	0°	90°
Modulus (GPa)	182.19 ± 3.195	11.30 ± 0.485
Strength (MPa)	1623.27 ± 66.255	107.37 ± 8.942

of 147.77 N at 1.99 mm displacement. As shown in Fig. 7 (E) the model predicts crack initiation on the tensile surface of the laminate and propagation through the laminate in the z-direction. The computed crack predictions are in good agreement with experimentally observed failure modes (Fig. 7(F)). It should be noted that inter-laminar delamination is not observed experimentally in 90° flexure tests. Again, this is correctly simulated by the model; computed inter-ply tractions are below the critical values, therefore cohesive zone delamination is not predicted to occur.

5.2. Predicting failure in compression tests of ± 45° laminates

Experimental results and computational predictions for compression tests performed on ± 45° laminates are presented in Fig. 8 below.

The experimentally measured stress-strain relationship is shown in Fig. 8 (A). The ± 45° laminates exhibit a linear elastic response followed by initial plastic yielding at a 0.2% proof stress of 92.5 MPa. Following initial yielding, the specimen undergoes strain hardening up to a compressive strain of 0.034; beyond this point the specified working limit of the strain gauges is exceeded and subsequent experimental strain data is not recorded. However, the ultimate compressive

strength of the laminate is measured as 213.19 ± 10.90 MPa, indicating that strain hardening continues beyond a strain of 0.034. A failure strain of 0.133 ± 0.016 is estimated from the test machine cross-head position, as indicated in Fig. 8 (A). The computational model provides an accurate prediction for the initial elastic behaviour and the post yield hardening behaviour. The yield point is strongly influence by the R_{12} value in the Hill model (Eq. (1)), again highlighting the importance of anisotropic plasticity for laminate structures. The model predicts that a crack initiates in the outermost plies at an applied nominal strain of 0.015 (Fig. 8 (Bi)) with crack propagation parallel to the fibre direction. Further loading does not result in crack propagation in the inner plies. The model also predicts that buckling and delamination of the outer plies occurs at an applied nominal strain of 0.04 (Fig. 8 (Bi)). Again, further loading does not result in delamination of inner plies and the laminate is predicted to support an increasing applied load until the equivalent plastic strain in the matrix exceeds the material ductility limit (0.48 (Rae et al., 2007)) in all ten plies (Fig. 8 (Dii)) at an applied strain of 0.17 with a predicted ultimate failure load of 218 MPa.

The predicted damage and failure mechanisms are supported by experimental test data (Fig. 8 (C)). Buckling and delamination are observed only in outer plies, in addition to crack growth parallel to the fibre direction. Additionally, experimental tests demonstrate that the laminate structure maintains its load bearing capacity up to an applied strain of 0.155; our model predicts that at such a high applied strain ductile failure due to excessive plastic deformation occurs in all plies.

5.3. Predicting failure in flexure tests of ± 45° laminates

Experimental results and computational predictions for flexure tests
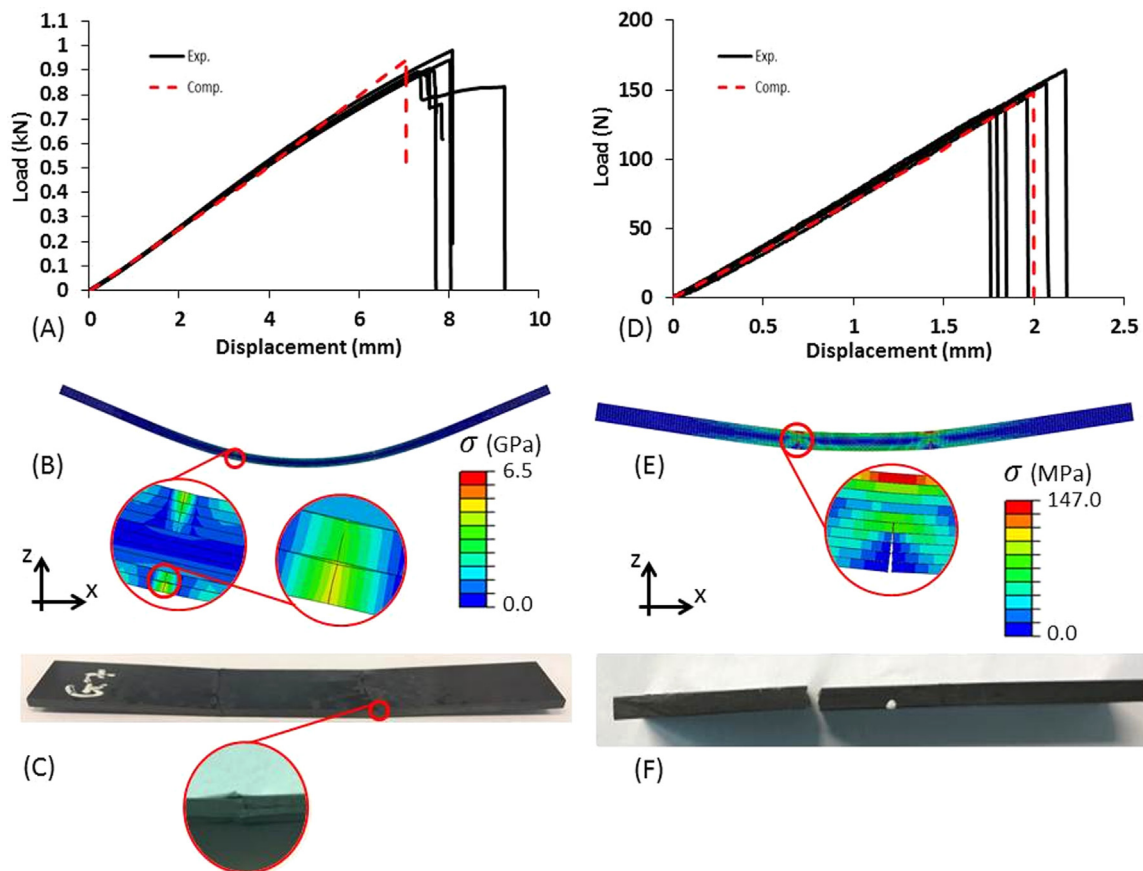

Fig. 7. (A) Experimental and computational force - displacement curves for flexure tests on 0° laminates. (B) Computational prediction of flexural failure in 0° laminates. (C) Experimental image of the failed 0° specimen. (D) Experimental and computational force - displacement curves for the 90° laminate. (E) Predicted von Mises stress (σ) distribution at failure. (F) Experimental image of a 90° flexure specimen following failure.
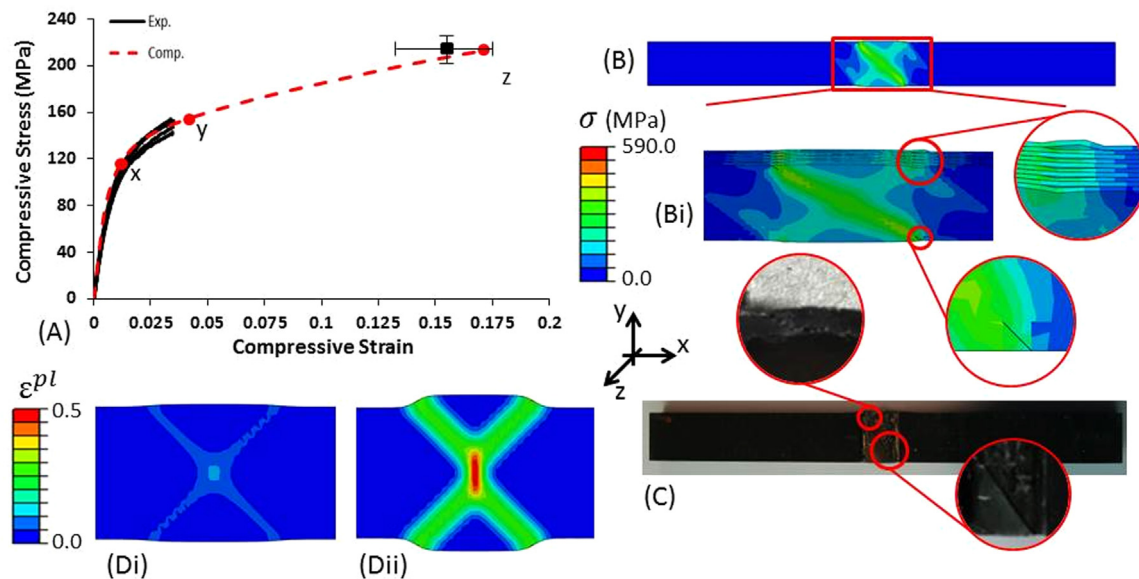
Fig. 8. A) Experimental and computational compressive stress – compressive strain curve for $\pm 45°$ laminates where (x) is the computed point of localised crack initiation in the outermost plies, (y) is the computed point of inter-laminar delamination onset and (z) is the point of ductile failure in all plies. B) Von Mises stress (σ) distribution in the computational model at the initiation of inter-laminar delamination. (Bi) Predicted locations for intra-laminar cracking and inter-laminar delamination. C) Experimental image of the $\pm 45°$ compression specimen at failure. (Di) Computed plastic strain distribution in the middle ply at the onset of delamination (at point y). (Dii) Predicted plastic strain distribution in the middle ply at failure.
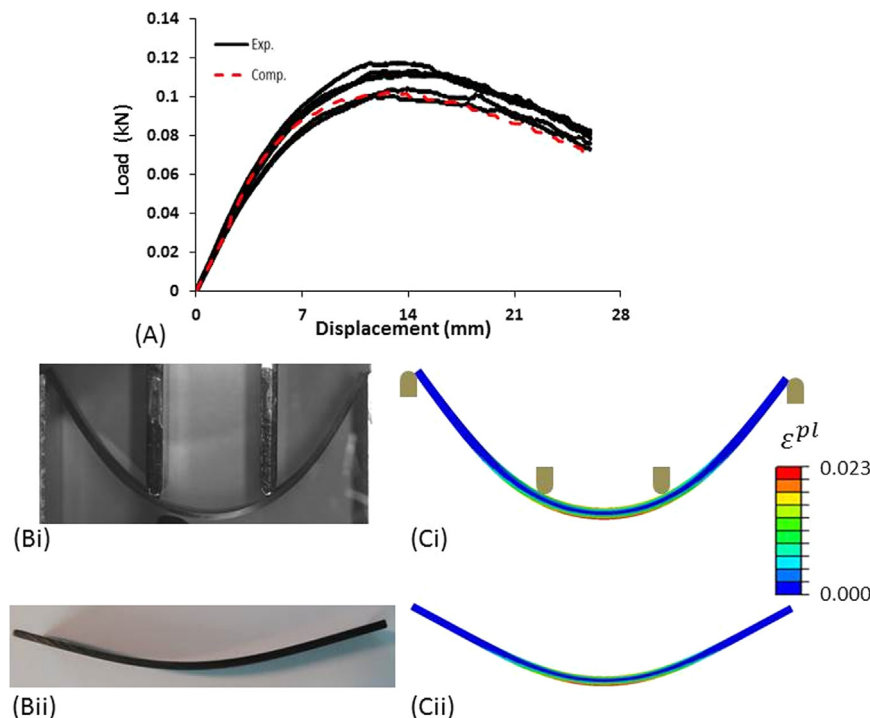

Fig. 9. (A) Experimental and computational force-displacement curve for the flexure test of $\pm 45°$ laminates. (Bi) Experimental image of $\pm 45°$ laminate at maximum deformation. (Bii) Experimental image of $\pm 45°$ laminate after unloading. (Ci) Predicted plastic strain (ε^{pl}) distribution at maximum deformation. (Cii) Predicted plastic deformation after unloading.

performed on $\pm 45°$ laminates are presented in Fig. 9 below.

Fig. 9 (A) shows the force-displacement diagram for $\pm 45°$ flexure test. The laminate exhibits linear-elastic behaviour up to initial plastic yielding at a 0.2% proof load of 70 N. After initial yielding, the specimen undergoes strain hardening up to a maximum force of 110.34 ± 0.63 N at an applied displacement of 13.07 ± 1.29 mm. The $\pm 45°$ laminates do not experience ultimate failure during the flexure tests. Rather, the samples continue to bend until the ends slide

between the fixed supports, as shown in Fig. 9 (Bi). No intra-laminar cracking or inter-laminar delamination is observed in the specimen. However permanent plastic deformation is observed upon removal of the applied load, as shown in Fig. 9 (Bii). The computational model accurately predicts the observed load-displacement behaviour (Fig. 9 (A)). The maximum load predicted by the computational model is 102.2 N at an applied displacement of 12.61 mm. Consistent with experimental observations, the model does not predict any delamination
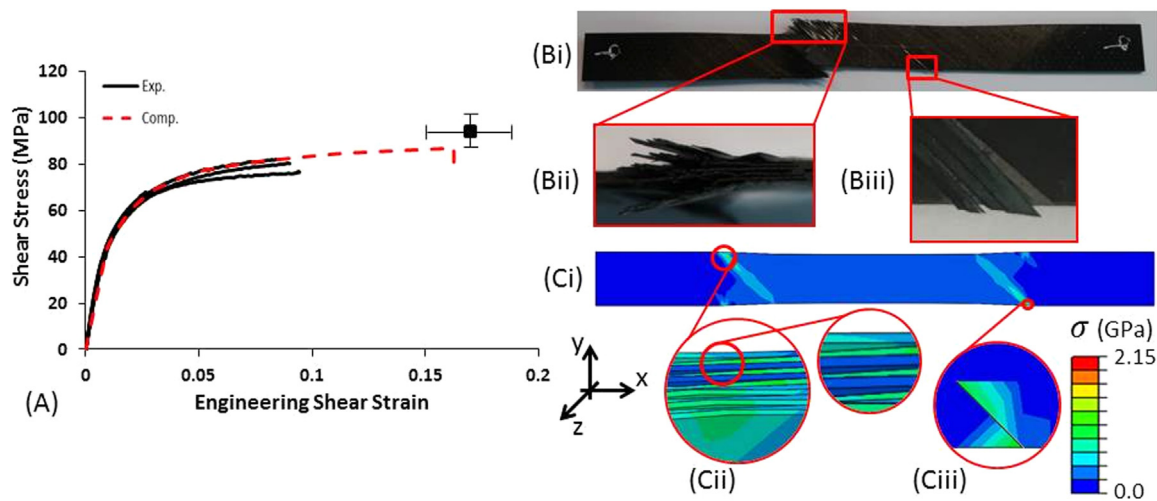
Fig. 10. (A) Experimental and computational shear stress - shear strain curves for the in-plane shear tests carried out on 45° laminates. (Bi) Experimental image of the ± 45° laminate at failure. (Bii) Experimental image of the delamination at failure. (Biii) Experimental image of matrix cracks propagating at 45° at failure. (Ci) Predicted von Mises stress (σ) distribution in the ± 45° laminate at failure. (Cii) Predicted inter-laminar delamination at failure. (Ciii) Predicted location of crack initiation.

or cracking. Finally, the model predicts significant plastic deformation upon load removal as shown in Fig. 9 (Cii), as observed experimentally.

5.4. Predicting failure in in-plane shear tests of ± 45° laminates

Results for in-plane shear (IPS) tests on ± 45° laminates are shown in Fig. 10.

Fig. 10 (A) shows the experimentally measured shear stress-shear strain relationship for the ± 45° laminate. A linear elastic region is observed up to a yield stress of 37.5 MPa, after which plastic deformation and strain hardening is observed. Measured strain data is plotted up to the specified limit of the strain gauges. Beyond this point, the specimen continues to undergo strain hardening up to a measured failure stress of 95.83 ± 7.44 MPa. A failure strain of 0.168 ± 0.031 is estimated from the crosshead displacement at failure, as indicated in Fig. 10 (A). The computational model provides an accurate prediction of the shear stress-shear strain behaviour, including the initial elastic region, initial plastic yielding and strain hardening. The model predicts that post yield hardening continues until failure at a shear stress of 86.9 MPa at an engineering shear strain of 0.162. Experimental images of a failed specimen (Fig. 10 (Bi)) reveal the complexity of failure in ± 45° laminates. Inter-laminar cracking parallel to the fibres (Fig. 10 (Biii)), in addition to inter-laminar delamination (Fig. 10 (Bii)), is observed. The model correctly predicts both the intra-laminar 45° cracks (Fig. 10 (Ciii)) and inter-laminar delamination (Fig. 10 (Cii)) in the same regions observed experimentally.

6. Preliminary device design

Next, we present an analysis of laminate plate performance under the physiological loading conditions of the femur. An adult femur (Isaza et al., 2013) is modelled with a mid-shaft fracture. The fracture is fixed with a locking compression plate (LCP) modelled on plates currently available in the market. The LCP (10 holes; length = 204 mm; width = 10 mm; thickness = 6.4 mm) is attached to the femur with rigid screws (diameter = 5 mm) in all 10 screw holes. Physiological joint forces and abductor muscle forces are applied to the proximal end of the femur (Özkaya et al., 2016; Polgár et al., 2003; Radcliffe and Taylor, 2007; Speirs et al., 2007). We assume that body weight (BW) is 70 kg, and during single leg stance the force acting through the femur head (F_J) and the muscle attachment point (F_M) is $|F_J|$ = 3.4 BW and $|F_M|$ = 2.6 BW, respectively. The fractured femur fixed with the LCP in plate is shown

in Fig. 11 (A), the boundary conditions for the femur during single leg stance are also illustrated (A).

Three different laminate layups are compared:

Laminate 1: $[0°_{16}]_s$, hereafter referred to as the 0° plate.
Laminate 2: $[\pm45°_4/0°_8]_s$, hereafter referred to as the 45°/0° plate.
Laminate 3: $[\pm45°_8]_s$, hereafter referred to as the 45° plate.

The stress distribution in the 0°, 45°/0° and 45° plates during single leg stance are shown in Fig. 11 (B), (C) and (D), respectively. In all three plates the areas of high stress are concentrated around the screw hole on the distal side of the fracture, with the highest stress predicted in the 0° plate. In the 45°/0° plate (Fig. 11(D)) it is clear that the 0° plies, located in the middle of the laminate and aligned with the femur shaft, are more highly stressed than the ± 45° plies located in the outermost plies of the laminate.

In Fig. 12 the laminated plates are loaded to failure to determine the load bearing capacity of each plate under physiological loading conditions. $|F_J|$ and $|F_M|$ are increased up to the point of failure while keeping a constant ratio of $|F_J|$ / $|F_M|$. Fig. 12(i) shows the relationship between the magnitude of F_J and the magnitude of the displacement of the femoral head relative to the fixed distal end of the femur. Clearly all three plates fail at loads greater than those associated with single leg stance. The 45° plate is the most compliant of the three plates, it fails at an applied joint load of 2.7 kN and a femur head displacement of 33.2 mm. The addition of the 0° plies to the ± 45° plies in the 45°/0° plate results in an increase in stiffness and an increase in the applied load at failure to 3.2 kN which is 1.4 times greater than loading associated with single leg stance. The 0° plate is the stiffest of the three plates and fails at an applied joint load of 3.7 kN, 1.6 times greater than applied loading during single leg stance, and femur head displacement of 33.3 mm.

As shown in Fig. 12(A) the compressive strength (-1183 MPa) is reached in the outermost ply on the medial side of the 0° plate and a crack forms. The 45°/0° plate (Fig. 12(B)) fails due to delamination at the interface of the 8th and 9th plies, where the 8th ply is a 45° ply and the 9th ply is a 0° ply. The change in stress concentration between the 0° ply and the 45° ply at that location (as highlighted in inset Fig. 11(B)) results in extensive inter-laminar failure. Similarly, the 45° ply (Fig. 12(C)) fails due to inter-laminar failure. Delaminations are predicted in multiple locations through the thickness of the laminate, as highlighted in the insert in Fig. 12(C).
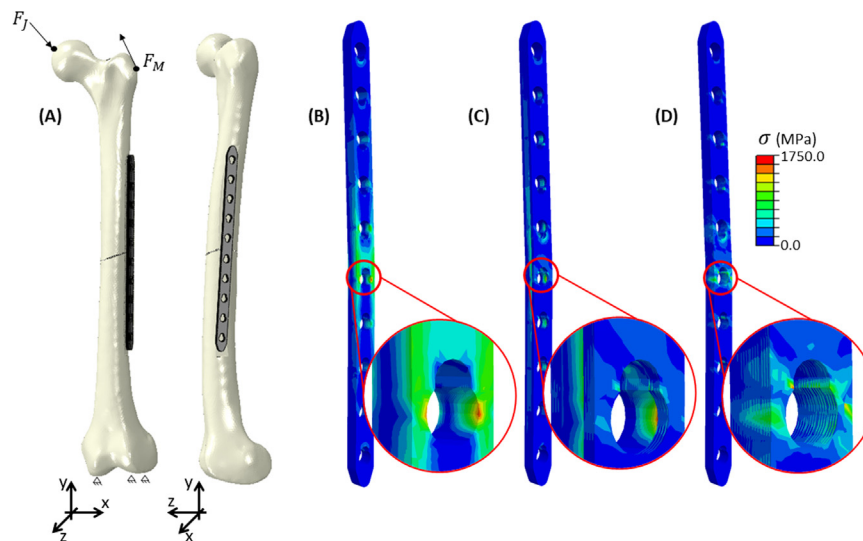
Fig. 11. (A) Femur geometry and attached LCP plate geometry with boundary conditions indicated. Contour plot of von Mises (σ) stress in the plate for single leg stance where $|F_J| = 2.335kN$ and $|F_M| = 1.785kN$ for; (B) 0° plate; (C) 45°/0° plate and (D) 45° plate.

The preliminary results demonstrate the importance of ply layup design for fracture fixation plates. It also demonstrates that all the failure mechanisms uncovered in Sections 4 and 5 of this study must be considered during the design of laminated fracture fixation plates.

7. Discussion

This paper presents, for the first time, experimental material characterisation of the medical grade unidirectional carbon fibre reinforced PEEK material, PEEK-OPTIMA™ Ultra-Reinforced. Due to the complex loading conditions applied to fracture fixation plates in the human body, it is essential that a comprehensive multi-axial characterisation of

material behaviour is performed in order to design reliable and safe implant devices. Our suite of multi-axial experimental tests uncovers three damage mechanisms: (1) inter-laminar delamination, (2) intra-laminar cracking and (3) anisotropic plasticity. A computational damage and failure model that incorporates all three modes of damage is developed and validated using our experimental data.

PEEK-OPTIMA™ Ultra-Reinforced has been cleared by the FDA for implantation in humans but to date no experimental test data has been published for the material. This presents a significant obstacle for safe design of first-generation laminated orthopaedic implants. In this study we present the first extensive material characterisation of PEEK-OPTIMA™ Ultra-Reinforced. In a previous study to determine the
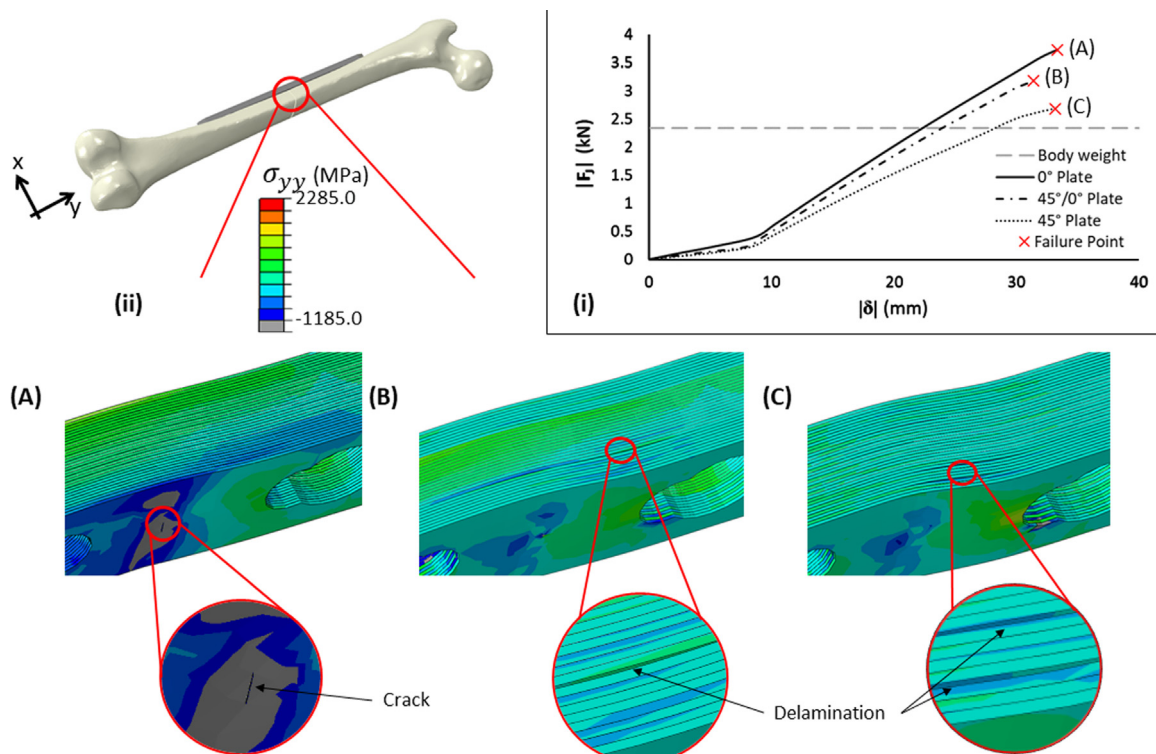

Fig. 12. (i) Graph of applied joint force ($|F_J|$) against displacement ($|\delta|$) of the femur head at the point of the applied joint force F_J, relative to the fixed distal end of the femur. (ii) Location of the close-up images of the longitudinal stress (σ_{yy}) distribution at failure for; (A) 0° plate; (B) 45°/0° plate and (C) 45° plate.

mechanical properties of a novel glass/flax/epoxy composite plate for long bone fracture fixation, tension, compression and three-point bend tests were performed (Bagheri et al., 2013; Manteghi et al., 2017). Studies on non-medical grade laminate materials have included compression and tension testing of 0° and 90° laminates and in-plane shear tests of ± 45° laminates (O'Higgins et al., 2008; Wonderly et al., 2005; Wu and Springer, 1988). In addition to such standard tests, the current study also presents extensive flexure testing of 0°, 90° and ± 45° laminates and mode I and mode II fracture toughness tests. Due to the complex multi-axial loading environment of orthopaedic implants, such an extensive suite of multi-axial experiments is necessary for safe device design. The preliminary device design presented in Section 6 of this study highlights the importance of ply layup design for the load bearing capacity of laminated fracture fixation plates. It also demonstrates how the computational framework developed in this study which combines anisotropic plasticity, inter-laminar and intra-laminar failure must be considered during the design of next generation laminated devices.

Experiments reveal the need for a complex multi-modal damage and failure model that includes: (1) inter-laminar delamination, (2) intra-laminar crack initiation and propagation and (3) anisotropic plasticity. Previous studies have developed computational damage models for non-medical grade laminate material. Such models have been limited to either the simulation of intra-laminar crack propagation (Ahmad et al., 2014; Duarte et al., 2017) or inter-laminar delamination (Heidari-Rarani et al., 2013; Turon et al., 2010; Zhao et al., 2014). Only the recent studies of Bouhala et al., Vigueras et al. and Grogan et al. (Bouhala et al., 2015; Grogan et al., 2015a, 2015b; Vigueras et al., 2015) have simulated combined intra-and inter-laminar failure. Furthermore only two studies that have included plasticity in their combined inter- intra-laminar failure models (Higuchi et al., 2017; van der Meer et al., 2011). A key deficiency of the van der Meer study is that only the off-axis non-linear responses in one loading direction are considered. Our suite of multi-axial experiments have shown that *CF/PEEK* has different yield points in different loading directions, it is impossible to accurately predict yielding in all directions if the yielding is only measured experimentally in one direction. In order to accurately simulate our experimental results we establish that anisotropic plasticity must be incorporated. Our model accurately predicts plastic yielding and strain hardening during compression loading of 90° la-

minates, and also during tension and compression loading of ± 45° laminates. Moreover, the model correctly predicts that fracture occurs without any plastic deformation in the case of tension and flexure loading of 0° and 90° laminates. By incorporating anisotropic plasticity in conjunction with inter-laminar delamination and intra-laminar crack propagation we accurately predict highly complex patterns of delamination evolution and laminate failure for a wide range of loading conditions, as observed in our experiments. The prediction of multi-axial multi-mode failure mechanisms is critical for the design of fibre reinforced laminated orthopaedic fracture fixation devices. Follow-on studies will consider additional multi-axial loading modes, and the influence of pressure-dependent yielding and mode dependent hardening (Vogler et al., 2013; Xue and Hutchinson, 2004) on laminate behaviour. Additionally, future studies should consider, cyclic loading, combined isotropic kinematic hardening plasticity formulation, fatigue failure and strain rate hardening.

In order to develop first-generation fibre reinforced laminated composite orthopaedic implants, the current paper makes two key contributions: (1) The first comprehensive experimental material characterisation of FDA cleared material PEEK-OPTIMA™ Ultra-Reinforced is presented; (2) A finite element framework that incorporates anisotropic plasticity in addition to inter-laminar delamination and intra-laminar cracks in order to accurately predict the complex failure mechanisms observed experimentally is developed. Follow-on studies will investigate the failure modes of laminates containing holes, laminated fracture fixation plate designs, and device-bone interface failure (Feerick and McGarry, 2012). Additionally, a micro-mechanical model will be developed to further investigate the modes of failure at the matrix-fibre interface.

Acknowledgements

Appendix A

The laminate layups and specimen dimensions are listed in Table A1.

Table A1
Specimen dimensions and layups for all of the tests outlined in the main body of this text.

Test	Standard	Layup	Test specimen dimensions		
			Length	Width	Thickness
Tension	ASTM 3039	$[0°]_5$	250.0	15.0	1.0
		$[90°]_{20}$	175.0	12.5	4.0
Compression	ASTM D6641	$[0°]_{10}$	140.0	12.0	2.0
		$[90°]_{10}$	140.0	12.0	2.0
		$[\pm45°]_5$	140.0	12.0	2.0
Flexure	ISO 14125	$[0°]_{10}$	100.0	15.0	2.0
		$[90°]_{10}$	60.0	15.0	2.0
		$[\pm45°]_5$	100.0	15.0	2.0
In-plane shear	ASTM D3518	$[\pm45°]_{s3}$	250.0	25.0	2.4
Fracture Toughness G_{ic} & G_{iic}	AECMA prEN6033 & prEN6034	$[0°]_{16}$	250.0	25.0	3.2

Appendix B

The equations used to calculate the mode I fracture toughness, G_{ic}, and the mode II fracture toughness, G_{iic}, are given in Eqs. (B1) and (B2),

respectively.

$$G_{ic} = \frac{A}{aw} \tag{B1}$$

$$G_{iic} = \frac{9Pda^2}{2w\left(\frac{L^3}{4}+3a^3\right)} \tag{B2}$$

where, A is the area under the force-displacement curve, a is the initial crack length, w is the width of the specimen, P is the load at the onset of crack propagation, d is the crosshead displacement at the onset of crack propagation and L is the length of the span.

A parameter study was carried out in order to determine the mode I and mode I interface strengths and the normal and tangential characteristic lengths for the cohesive zone model. The results are presented in Fig. B1.

Fig. B1 (B) shows the results of the parameter study performed to determine cohesive zone properties for the mode I inter-laminar strength (σ_{max}) and the normal characteristic interface length (Δ_n). The peak force is governed by both σ_{max} and Δ_n. The plateau in force that occurs after propagation is highly influenced by the value of σ_{max}. Increasing σ_{max} results in the plateau occurring at higher force and vice versa. Fig. B1 (B) shows the results of the parameter study performed to determine cohesive zone properties for the mode II inter-laminar strength (τ_{max}) and the tangential characteristic interface length (Δ_t). Examining the force-displacement relationships it is evident that the peak force is highly influenced by τ_{max}, increasing τ_{max} causes an increase in the max force. The slope of the curve and the drop in force after the crack has begun to propagate are primarily governed by Δ_t.
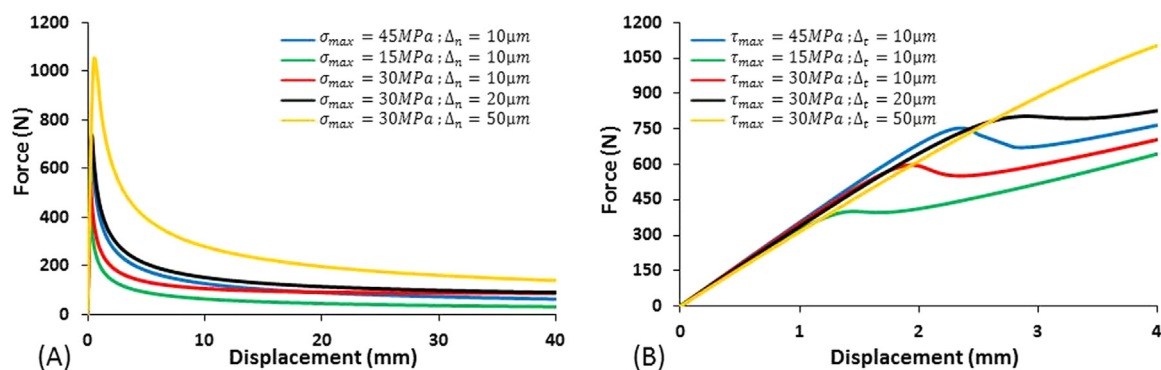

Fig. B1. (A) Force-displacement curves for different mode I cohesive zone parameters. (B) Force-displacement curves for different mode II cohesive zone parameters.

References

AECMA Standard, 1995a. prEN 6033 Aerospace series Carbon fibre reinforced plastics Test method Determination of interlaminar fracture toughness energy Mode I.

AECMA Standard, 1995b. prEN 6034 Aerospace series Carbon fibre reinforced plastics Test method Determination of interlaminar fracture toughness energy Mode II.

Ahmad, H., Crocombe, A.D., Smith, P.A., 2014. Strength prediction in CFRP woven laminate bolted single-lap joints under quasi-static loading using XFEM. Compos. Part A Appl. Sci. Manuf. 66, 82–93. http://dx.doi.org/10.1016/j.compositesa.2014.07.013.

Aitasalo, K.M.J., Piitulainen, J.M., Rekola, J., Vallittu, P.K., 2014. Craniofacial bone reconstruction with bioactive fiber-reinforced composite implant. Head Neck 36, 722–728. http://dx.doi.org/10.1002/hed.23370.

ASTM International, 2014. ASTM D3039/D3039M: Standard test method for tensile properties of polymer matrix composite materials. Annu. B. ASTM Stand. ⟨https://dx.doi.org/10.1520/D3039⟩.

ASTM International, 2013. ASTM D3518/D3518M Standard Test Method for In-Plane Shear Response of Polymer Matrix Composite Materials by Tensile Test of a 45 ˚ Laminate. Annu. B. ASTM Stand. ⟨https://dx.doi.org/10.1520/D3518⟩.

ASTM International, 2012. ASTM D6641/D6641M Standard Test Method for Compressive Properties of Polymer Matrix Composite Materials Using a Combined Loading Compression (CLC). Annu. B. ASTM Stand. i, 1–11. ⟨https://dx.doi.org/10.1520/D6641⟩.

Bagheri, Z.S., El Sawi, I., Schemitsch, E.H., Zdero, R., Bougherara, H., 2013. Biomechanical properties of an advanced new carbon/flax/epoxy composite material for bone plate applications. J. Mech. Behav. Biomed. Mater. 20, 398–406. http://dx.doi.org/10.1016/j.jmbbm.2012.12.004.

Ballo, A.M., Lassila, L.V., Vallittu, P.K., Närhi, T.O., 2007. Load bearing capacity of bone anchored fiber-reinforced composite device. J. Mater. Sci. Mater. Med. 18, 2025–2031. http://dx.doi.org/10.1007/s10856-007-3159-6.

Bieniaś, J., Dębski, H., Surowska, B., Sadowski, T., 2012. Analysis of microstructure damage in carbon/epoxy composites using FEM. Comput. Mater. Sci. 64, 168–172. http://dx.doi.org/10.1016/j.commatsci.2012.03.033.

Bouhala, L., Makradi, A., Belouettar, S., Younes, A., Natarajan, S., 2015. An XFEM/CZM based inverse method for identification of composite failure parameters. Comput. Struct. 153, 91–97. http://dx.doi.org/10.1016/j.compstruc.2015.02.035.

Brantigan, J.W., Steffee, A.D., 1993. A carbon fiber implant to aid interbody lumbar fusion (Phila. Pa. 1976). Spine 18, 2106–2117. http://dx.doi.org/10.1097/00007632-199310001-00030.

Der Tavitian, J., Davison, J.N.S., Dias, J.J., 2002. Clavicular fracture non-union surgical outcome and complications. Injury 33, 135–143. http://dx.doi.org/10.1016/S0020-1383(01)00069-9.

Duarte, A.P.C., Díaz Sáez, A., Silvestre, N., 2017. Comparative study between XFEM and Hashin damage criterion applied to failure of composites. Thin-Walled Struct. 115, 277–288. http://dx.doi.org/10.1016/j.tws.2017.02.020.

Feerick, E.M., Kennedy, J., Mullett, H., FitzPatrick, D., McGarry, P., 2013a. Investigation of metallic and carbon fibre PEEK fracture fixation devices for three-part proximal humeral fractures. Med. Eng. Phys. 35, 712–722. http://dx.doi.org/10.1016/j.medengphy.2012.07.016.

Feerick, E.M., Liu, X.C., McGarry, P., 2013b. Anisotropic mode-dependent damage of cortical bone using the extended finite element method (XFEM). J. Mech. Behav. Biomed. Mater. 20, 77–89. http://dx.doi.org/10.1016/j.jmbbm.2012.12.004.

Feerick, E.M., McGarry, J.P., 2012. Cortical bone failure mechanisms during screw pullout. J. Biomech. 45, 1666–1672. http://dx.doi.org/10.1016/j.jbiomech.2012.03.023.

Feerick, E.M., Wilson, J., Jarman-Smith, M., Ó'Brádaigh, C.M., McGarry, J.P., 2014. Self-tapping ability of carbon fibre reinforced polyetheretherketone suture anchors. J. Biomater. Appl. 29, 502–513. http://dx.doi.org/10.1177/0885328214535274.

Gallagher, E., Ó'Brádaigh, C.M., McGarry, J.P., 2015. A computational investigation into the use of carbon fibre reinforced PEEK laminates for orthopaedic applications. In: Proceedings of the 2nd International PEEK Meeting. Washinton D.C, p. 60.

Grogan, D.M., Ó Brádaigh, C.M., Leen, S.B., 2015a. A combined XFEM and cohesive zone model for composite laminate microcracking and permeability. Compos. Struct. 120, 246–261. http://dx.doi.org/10.1016/j.compstruct.2014.09.068.

Grogan, D.M., Ó Brádaigh, C.M., McGarry, J.P., Leen, S.B., 2015b. Damage and permeability in tape-laid thermoplastic composite cryogenic tanks. Compos. Part A Appl. Sci. Manuf. 78, 390–402. http://dx.doi.org/10.1016/j.compositesa.2015.08.037.

Hashin, Z., 1980a. Failure criteria for unidirectional fiber composites. J. Appl. Mech. 47, 329. http://dx.doi.org/10.1115/1.3153664.

Heidari-Rarani, M., Shokrieh, M.M., Camanho, P.P., 2013. Finite element modeling of mode i delamination growth in laminated DCB specimens with R-curve effects. Compos. Part B Eng. 45, 897–903. http://dx.doi.org/10.1016/j.compositesb.2012.09.051.

Higuchi, R., Okabe, T., Nagashima, T., 2017. Numerical simulation of progressive damage and failure in composite laminates using XFEM/CZM coupled approach. Compos. Part A Appl. Sci. Manuf. 95, 197–207. http://dx.doi.org/10.1016/j.compositesa.2016.12.026.

Huiskes, R., Weinans, H., van Rietbergen, B., 1992. The relationship between stress shielding and bone resorption around total hip stems and the effects of flexible materials. Clin. Orthop. Relat. Res. 124–134. http://dx.doi.org/10.1097/00003086-199201000-00014.

Isaza, E., García, L., Salazar, E., 2013. Determination of Mechanic Resistance of Osseous Element through Finite Element Modeling, In: COMSOL Conference. pp. 1–7.

ISO, 1998. Fibre-Reinforced Plastic Composites Determination of Flexural Properties. 〈https://dx.doi.org/10.1520/E0872-82R13.2〉.

Kurtz, S.M., Devine, J.N., 2007. PEEK biomaterials in trauma, orthopedic, and spinal implants. Biomaterials 28, 4845–4869. http://dx.doi.org/10.1016/j.biomaterials.2007.07.013.

Lanzetta, M., Foucher, G., 1995. A comparison of different surgical techniques in treating degenerative arthrosis of the carpometacarpal joint of the thumb: a retrospective study of 98 cases. J. Hand Surg. (Br. Eur. 20, 105–110. http://dx.doi.org/10.1016/S0266-7681(05)80027-0.

Lessard, L.B., Chang, F., 1991. Damage tolerance of laminated composites containing an open hole and subjected to tensile loadings: patr II-experiment. J. Compos. Mater. 25, 44–64. http://dx.doi.org/10.1177/002199839102500303.

Li, C., Granger, C., Del Schutte, H., Biggers, S.B., Kennedy, J.M., Latour, R.A., 2002. Progressive failure analysis of laminated composite femoral prostheses for total hip arthroplasty. Biomaterials 23, 4249–4262.

Manteghi, S., Mahboob, Z., Fawaz, Z., Bougherara, H., 2017. Investigation of the mechanical properties and failure modes of hybrid natural fiber composites for potential bone fracture fixation plates. J. Mech. Behav. Biomed. Mater. 65, 306–316. http://dx.doi.org/10.1016/j.jmbbm.2016.08.035.

McGarry, J.P., Ó Máirtín, É., Parry, G., Beltz, G.E., 2014. Potential-based and non-potential-based cohesive zone formulations under mixed-mode separation and overclosure. Part I: theoretical analysis. J. Mech. Phys. Solids 63, 336–362. http://dx.doi.org/10.1016/j.jmps.2013.08.020.

O'Brien, T.K., 1982. Characterization of delamination onset and growth in a composite laminate. Damage Compos. Mater. Basic Mech. Accumul., Toler. Charact. 140–167. http://dx.doi.org/10.1520/STP34325S.

O'Higgins, R.M., McCarthy, M.A., McCarthy, C.T., 2008. Comparison of open hole tension characteristics of high strength glass and carbon fibre-reinforced composite materials. Compos. Sci. Technol. 68, 2770–2778. http://dx.doi.org/10.1016/j.compscitech.2008.06.003.

Özkaya, N., Goldsheyder, D., Nordin, M., Leger, D., 2016. Fundamentals of biomechanics: Equilibrium, motion, and deformation, fourth edition, Fundamentals of Biomechanics: Equilibrium, Motion, and Deformation, Fourth Edition. 〈https://dx.doi.org/10.1007/978-3-319-44738-4〉.

Piitulainen, J.M., Kauko, T., Aitasalo, K.M.J., Vuorinen, V., Vallittu, P.K., Posti, J.P., 2015. Outcomes of cranioplasty with synthetic materials and autologous bone grafts. World Neurosurg. http://dx.doi.org/10.1016/j.wneu.2015.01.014.

Polgár, K., Gill, H.S., Viceconti, M., Murray, D.W., O'Connor, J.J., 2003. Strain distribution within the human femur due to physiological and simplified loading: finite element analysis using the muscle standardized femur model. Proc. Inst. Mech. Eng. Part H J. Eng. Med. 217, 173–189. http://dx.doi.org/10.1243/095441103765212677.

Pozegic, T.R., Anguita, J.V., Hamerton, I., Jayawardena, K.D.G.I., Chen, J.-S., Stolojan, V., Ballocchi, P., Walsh, R., Silva, S.R.P., 2016. Multi-functional carbon fibre composites using carbon nanotubes as an alternative to polymer sizing. Sci. Rep. 6, 37334. http://dx.doi.org/10.1038/srep37334.

Puck, A., Schürmann, H., 2002. Failure analysis of FRP laminates by means of physically based phenomenological models. Compos. Sci. Technol. 62, 1633–1662. http://dx.doi.org/10.1016/S0266-3538(96)00140-6.

Radcliffe, I.A.J., Taylor, M., 2007. Investigation into the effect of varus-valgus orientation on load transfer in the resurfaced femoral head: a multi-femur finite element analysis. Clin. Biomech. 22, 780–786. http://dx.doi.org/10.1016/j.clinbiomech.2007.03.011.

Rae, P.J., Brown, E.N., Orler, E.B., 2007. The mechanical properties of poly(ether-ether-ketone) (PEEK) with emphasis on the large compressive strain response. Polymer 48, 598–615. http://dx.doi.org/10.1016/j.polymer.2006.11.032.

Soden, P.D., Hinton, M.J., Kaddour, A.S., 2004. Lamina properties, lay-up configurations and loading conditions for a range of fibre reinforced composite laminates. Fail. Criteria Fibre-Reinf.-Polym. Compos. 30–51. http://dx.doi.org/10.1016/B978-008044475-8/50003-2.

Speirs, A.D., Heller, M.O., Duda, G.N., Taylor, W.R., 2007. Physiologically based boundary conditions in finite element modelling. J. Biomech. 40, 2318–2323. http://dx.doi.org/10.1016/j.jbiomech.2006.10.038.

Tsai, S.W., Wu, E.M., 1971. A general theory of strength for anisotropic materials. J. Compos. Mater. 5, 58–80. http://dx.doi.org/10.1177/002199837100500106.

Turon, A., Camanho, P.P., Costa, J., Renart, J., 2010. Accurate simulation of delamination growth under mixed-mode loading using cohesive elements: definition of interlaminar strengths and elastic stiffness. Compos. Struct. 92, 1857–1864. http://dx.doi.org/10.1016/j.compstruct.2010.01.012.

van der Meer, F., Sluys, L., Hallett, S., Wisnom, M., 2011. Computational modeling of complex failure mechanisms in laminates. J. Compos. Mater. 46, 603–623. http://dx.doi.org/10.1177/0021998311410473.

Van Paepegem, W., De Baere, I., Degrieck, J., 2006. Modelling the nonlinear shear stress-strain response of glass fibre-reinforced composites. Part I: experimental results. Compos. Sci. Technol. 66, 1455–1464. http://dx.doi.org/10.1016/j.compscitech.2005.04.014.

Vigueras, G., Sket, F., Samaniego, C., Wu, L., Noels, L., Tjahjanto, D., Casoni, E., Houzeaux, G., Makradi, A., Molina-Aldareguia, J.M., Vázquez, M., Jérusalem, A., 2015. An XFEM/CZM implementation for massively parallel simulations of composites fracture. Compos. Struct. 125, 542–557. http://dx.doi.org/10.1016/j.compstruct.2015.01.053.

Vogler, M., Rolfes, R., Camanho, P.P., 2013. Modeling the inelastic deformation and fracture of polymer composites-Part I: plasticity model. Mech. Mater. 59, 50–64. http://dx.doi.org/10.1016/j.mechmat.2012.12.002.

Wisnom, M.R., Hallett, S.R., 2009. The role of delamination in strength, failure mechanism and hole size effect in open hole tensile tests on quasi-isotropic laminates. Compos. Part A Appl. Sci. Manuf. 40, 335–342. http://dx.doi.org/10.1016/j.compositesa.2008.12.013.

Wonderly, C., Grenestedt, J., Fernlund, G., Cěpus, E., 2005. Comparison of mechanical properties of glass fiber/vinyl ester and carbon fiber/vinyl ester composites. Compos. Part B Eng. 36, 417–426. http://dx.doi.org/10.1016/j.compositesb.2005.01.004.

Wu, H.-Y.T., Springer, G.S., 1988. Measurements of matrix cracking and delamination caused by impact on composite plates. J. Compos. Mater. 22, 518–532. http://dx.doi.org/10.1177/002199838802200602.

Xue, Z., Hutchinson, J.W., 2004. Constitutive model for quasi-static deformation of metallic sandwich cores. Int. J. Numer. Methods Eng. 61, 2205–2238. http://dx.doi.org/10.1002/nme.1142.

Zhao, L., Gong, Y., Zhang, J., Chen, Y., Fei, B., 2014. Simulation of delamination growth in multidirectional laminates under mode I and mixed mode I/II loadings using cohesive elements. Compos. Struct. 116, 509–522. http://dx.doi.org/10.1016/j.compstruct.2014.05.042.